Meccanica (2025) 60:3407–3427
https://doi.org/10.1007/s11012-024-01913-z

RESEARCH

Compensated velocity feedback for non-collocated active vibration control

Natasha Hirschfeldt · Thomas Furtmüller · Christoph Adam · Roland Maderebner

Received: 2 September 2024 / Accepted: 11 November 2024 / Published online: 24 December 2024

Abstract This paper addresses non-collocated vibration control of multi-modal structures such as plates. The challenges of applying this non-collocated configuration in real systems are tackled by proposing a second-order compensator using velocity feedback control. The compensator design aims to use uncontrolled data only, where its parameters are obtained from a measurement of the point-frequency response function at the actuator attachment point (anti-resonance assignment). Compared to other control strategies such as optimal control, no plant model or state estimation is required in the hardware implementation of the controller, making this approach relatively simple. The compensator design is outlined for a generic three-degree-of-freedom system, as its simplicity allows for deeper investigation of the effects of the compensator itself. The proposed design is then experimentally validated by vibration control of a cross-laminated timber panel, considering three closely spaced natural frequencies. Further difficulties encountered in dealing with real world systems are discussed by comparing experimental data with simulations. To achieve this, a model of the electromechanical system composed of the panel and two electrodynamic shakers is used. The parameters of the compensator for the system are then obtained and a sensitivity study to these parameters is carried out by calculating a control performance taking into account filters and the effects of time delay.

Keywords Active vibration control · Anti-resonance assignment · Cross-laminated timber panel · Non-collocated control · Transmission zeroes · Velocity feedback

N. Hirschfeldt · T. Furtmüller · C. Adam (✉)
Universität Innsbruck, Unit of Applied Mechanics, Technikerstr. 13, 6020 Innsbruck, Austria
e-mail: christoph.adam@uibk.ac.at

N. Hirschfeldt
e-mail: natasha.hirschfeldt@uibk.ac.at

T. Furtmüller
e-mail: thomas.furtmueller@uibk.ac.at

R. Maderebner
Universität Innsbruck, Unit of Timber Engineering, Technikerstr. 13, 6020 Innsbruck, Austria
e-mail: roland.maderebner@uibk.ac.at

1 Introduction

Vibration control is a wide field of study that aims to modify the dynamic response of a system as desired. This can be achieved by passive approaches, active approaches or a combination of both. Studies on these approaches are extensive and can be found, for example, in [1–5]. Passive control is achieved, for instance, by adding a mechanical element to the structure to be controlled. From approaches such as an inerter-based absorbers [6] to the use of piezoelectric layers with attached electric circuits [7], passive control is widely used in structural control. A usual application of this

type of control is through elements such as a tuned mass damper (TMD). This mass-spring-damper system is tuned to a target frequency [1, 8], typically the fundamental natural frequency. Since it does not rely on an external energy source to achieve vibration mitigation, passive control is inherently stable. However, its efficiency depends highly on the proper tuning of the TMD frequency and TMD damping, which becomes even more challenging when more than one vibration mode of the structure is to be controlled with multiple TMDs. Furthermore, since passive devices can be quite large and heavy, they may not be practical to implement, for example, in lightweight structures. In these cases, active control is more favorable.

In active control, an actuator interferes with the structure to be controlled, whose input signal is generated based on measurement data from a sensor attached to the structure. Several control approaches can be used for active vibration control, such as acceleration feedback [9], PD controllers [10], linear quadratic regulator [1], model predictive control [11], time-delayed vibration absorbers [12], pole placement [13], and modal filters [14]. Due to its simplicity in terms of hardware implementation, direct velocity feedback [15, 16] has been a widely used approach in active vibration control applications whose implications are still being discussed in the literature [17]. In the present paper, velocity feedback will be discussed in more detail.

In a single input-single output (SISO) layout, collocated and non-collocated configurations can be distinguished. Control is referred to as collocated when the sensor-actuator pair is located at the same position in a structure as the actuator that applies the control. Due to its inherent stability, collocated control has been extensively studied [8, 9, 15, 16, 18, 19]. However, collocated setups are often difficult to achieve in practice, either because of a slight positional mismatch between sensor and actuator, or because of the inaccessibility of the target position. Therefore, the study of non-collocated control, i.e. the sensor and actuator are located at different positions, is of interest [1, 14, 20]. In [14], a modal filter of second-order is proposed for non-collocated control of flexible structures, with good high-frequency roll-off characteristics. In [21], a positive position feedback algorithm in a non-collocated setup of a free sandwich plate is examined. The study shows that greater amplitude reduction is achieved by non-collocated control compared to collocated control. In [22], a filtered velocity feedback control is used to overcome instabilities caused by the non-collocated configuration in the control system, which is achieved by combining direct velocity feedback with positive position feedback. Other approaches can also be used, such as the receptance method, which requires only the available states of the system to complete the equations, while the usual state-space approach requires all states to be known (by measurement or estimation by an observer). In [23], the receptance method for output-feedback is used for collocated vibration control by eigenvalue assignment, where no prior knowledge of the system matrices is required, using only measured receptances from the open-loop system.

The assignment of poles and zeroes for vibration reduction is a widely used technique in control theory. For example, [24] uses transmission zeroes to propose a criterion for the optimal placement of a collocated set of sensor and actuator to maximize the modal damping ratio for target modes. Other studies, such as [13] present a control design method for the assignment of poles and zeroes for linear time-invariant systems in the context of non-collocated vibration control. The methodology employed by [25] is to set the anti-resonance frequency (corresponding to a transmission zero in the Laplace domain) to the same value as the force excitation frequency for non-collocated vibration control. In contrast, [26] focuses on maximizing the stability margin of a control system while assigning transmission zeroes on the imaginary axis.

In the present paper, a cross-laminated timber (CLT) panel is used as the structure to be controlled. CLT is a structural element composed of glued timber layers, usually made of an odd number of layers arranged perpendicular to each other [27]. Due to this configuration, CLT panels can support in-plane and out-of-plane loads and can therefore be used as floors and walls. Compared to conventional structures made of concrete or steel, CLT structures are considered light-weight, which makes them more prone to vibrations. This can cause discomfort to people, making the study of vibration control of CLT elements of great interest [28]. Studies on the reduction of floor vibrations can be found in [8, 9, 15, 16, 29, 30].

In this paper, active vibration control is approached through velocity feedback control, which aims to

attenuate the amplitude of the system response around resonance peaks by providing active damping. Non-collocated control is considered, where a new assignment of zeroes is proposed to cope with the instabilities caused by this configuration. Unlike [25, 26], which use extensive mathematical operations and require a model of the system to be controlled, the present solution is direct and requires neither a model nor an estimation of states. A compensator is proposed that is designed based solely on antiresonance information about the uncontrolled system, making its implementation simple and easily applicable to real systems.

The paper is organized as follows. In sect.2, the necessary basics for non-collocated configurations and the design of compensators are presented using the example of a three-degree-of-freedom (3 DoF) system. The application of the compensator, which is demonstrated by experiments, is presented in sect.3, considering a CLT panel and two electrodynamic shakers. Both the experimental results and the modeling as well as system identification of the entire electromechanical system are discussed. In sect.4, conclusions are drawn with respect to the control system with the proposed compensator.

2 Problem statement

2.1 Generic setup

Consider the generic mass-spring-damper system depicted in Fig. 1, which is composed of three single-degree-of-freedom oscillators connected in series with lumped masses m_1, m_2, m_3, linear elastic springs with stiffness k_1, k_2, k_3, and viscous dampers b_1, b_2, b_3. The degrees-of-freedom are the displacements $x_1(t), x_2(t), x_3(t)$ of each mass, respectively, and the external disturbance is provided by a force $f_1(t)$ applied to the mass m_1. The coupled equations of motion of the uncontrolled 3 DoF system in its general form is

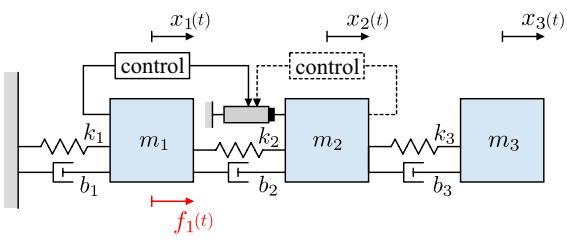

Fig. 1 Collocated (dashed line) and non-collocated (solid line) configurations of a 3 DoF control system

$$\mathbf{M}\,\ddot{\mathbf{x}}(t) + \mathbf{C}\,\dot{\mathbf{x}}(t) + \mathbf{K}\,\mathbf{x}(t) = \mathbf{f}(t) \tag{1}$$

where $\mathbf{x}(t) = [x_1(t)\ \ x_2(t)\ \ x_3(t)]^T$, $\mathbf{f}(t) = [f_1(t)\ \ 0\ \ 0]^T$ and $\mathbf{M}, \mathbf{C}, \mathbf{K}$ are the mass matrix, damping matrix and stiffness matrix, respectively.

It is possible to write Eq. (1) in terms of the modal coordinates $y_k(t)$ [31–33] as

$$x_n(t) = \sum_{k=1}^{3} \boldsymbol{\phi}_{kn}\, y_k(t) \tag{2}$$

where $\boldsymbol{\phi}_{kn}$ is the mode shape of the kth mode ($k = 1, 2, 3$) for degree-of-freedom n ($n = 1, 2, 3$). The equations of motion then become

$$\tilde{\mathbf{M}}\,\ddot{\mathbf{y}}(t) + \tilde{\mathbf{C}}\,\dot{\mathbf{y}}(t) + \tilde{\mathbf{K}}\,\mathbf{y}(t) = \boldsymbol{\Phi}^T\mathbf{f}(t) \tag{3}$$

where $\boldsymbol{\Phi}$ is the modal coefficient matrix and $\tilde{\mathbf{M}}, \tilde{\mathbf{C}}, \tilde{\mathbf{K}}$ are the modal mass matrix, damping matrix and stiffness matrix, respectively. Assuming modal damping - which, strictly speaking, contradicts the model definition by means of arbitrary damper coefficients b_k, but is a good approximation for lightly damped systems - Eq. (3) can be written as a set of three uncoupled modal oscillators,

$$\ddot{y}_k(t) + 2\xi_k\omega_k\dot{y}_k(t) + \omega_k^2 y_k(t) = \frac{1}{\tilde{m}_k}\phi_{k1}f_1(t) \tag{4}$$

where $\tilde{m}_k$ is the modal mass, ω_k is the undamped natural frequency, ξ_k the damping ratio and $\boldsymbol{\phi}_{k1}$ are the modal coefficients at DoF 1. The Laplace transform of Eq. (4) is

$$s^2\ Y_k(s) + 2\xi_k\omega_k s\ Y_k(s) + \omega_k^2\ Y_k(s) = \frac{1}{\tilde{m}_k}\phi_{k1}F_1(s) \tag{5}$$

where capital letters denote the Laplace transformed variable from time domain. Considering the transformation to physical coordinates through Eq. (2), the transfer function from the input force f_1 to the output quantity acceleration $a_n \equiv \ddot{x}_n$ is

$$H_{n1}(s) = \frac{A_n(s)}{F_1(s)} = \frac{s^2X_n(s)}{F_1(s)} = \sum_{k=1}^{3} \frac{\phi_{kn}\phi_{k1}s^2}{\tilde{m}_k(s^2 + 2\xi_k\omega_k s + \omega_k^2)} \tag{6}$$

Values of s that make the denominator of Eq. (6) go to zero are called poles, while zeroes (or transmission zeroes) are the values of s that make the transfer function Eq. (6) go to zero [1, 34, 35]. Both assume complex values and have a clear physical meaning. In the case of a pole, its imaginary part is the (damped) natural frequency while for a zero the imaginary part corresponds to the frequency at which a non-zero input leads to a zero output, i.e. an anti-resonance, where there is a cancellation of the contribution of modes between two resonance peaks (but not a complete cancellation in the case of a damped system). Zeroes provide a phase lead to the system, which compensates the phase lag from a pole [1, 34].

The concept of poles and zeroes is widely used in control theory and stability analysis. For example, the closed-loop poles of a control system tend toward the open-loop zeroes for infinite feedback gain. Instability of the control system occurs when at least one pole assumes a positive real part for any feedback gain.

2.2 Velocity feedback control

For vibration control, an actuator is attached to the structure, which is shown as a gray rectangle in Fig. 1 and is positioned so that it actuates on m_2 (DoF x_2). Both a collocated and a non-collocated configuration are considered. In the collocated case, information about the motion of m_2 is transmitted to the actuator, while in the non-collocated configuration, information about the motion of m_1 is used. In the following, it is assumed that the measured accelerations of these masses $a_2(t)$ and $a_1(t)$ provide this information, as accelerometers are usually used as sensors in practice. In velocity feedback control, the actuator supplies the system with the counteracting force $f_c(t)$ proportional to the measured velocity by integrating the acceleration signal. The Laplace transform of the control law reads

$$F_c(s) = G(s)A_n(s) = g\frac{1}{s}A_n(s) \quad \text{with} \quad G(s) = g\,\frac{1}{s} \tag{7}$$

where $n = 1$ for the non-collocated control and $n = 2$ for the collocated control. g is the scalar gain value.

2.3 Collocated vs. non-collocated control

The following simulations consider the 3 DoF system shown in Fig. 1 with equal stiffness coefficients $k_1 = k_2 = k_3 = 6000$ N/m, unit masses $m_n = 1$ kg as well as a low damping $\xi_1 = \xi_2 = \xi_3 = 0.02$. It is also assumed at this point that the actuator has ideal dynamics and is therefore not considered in the modeling of the system. In this case, the force vector $\mathbf{f}(t) = [f_1(t)\ \ f_c(t)\ \ 0]^T$ in Eq. (1) includes both the external disturbance and the actuator force.

Figure 2 shows block diagrams for both collocated and non-collocated configurations, where $H_{21}(s), H_{22}(s), H_{11}(s)$ and $H_{12}(s)$ are open-loop transfer functions defined analogously to Eq. (6). Since the disturbance F_1 is always assumed at DoF x_1, the input branches in the block diagrams for the target points of vibration mitigation (DoFs x_2 and x_1, respectively) are represented by the transfer functions $H_{21}(s)$ and $H_{11}(s)$, respectively. Meanwhile, the control branches use $H_{22}(s)$ and $H_{12}(s)$, which represent the relationships between the actuator input at DoF x_2 and the target points. Considering the block diagram for the collocated control shown on the left of Fig. 2, the counteracting force provided by the actuator in Eq. (7) results in the closed-loop transfer function

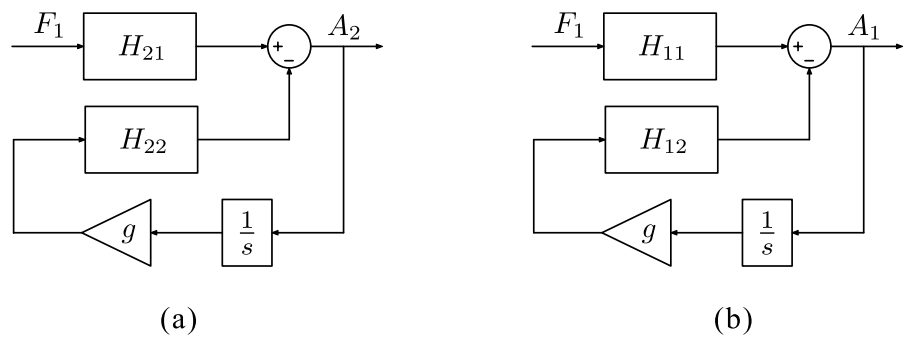

Fig. 2 Block diagrams for: **a** collocated configuration and **b** non-collocated configuration

$$H_{21}^{cl}(s) = \frac{A_2(s)}{F_1(s)} = \frac{H_{21}(s)}{1 + G(s)H_{22}(s)} \tag{8}$$

Figure 3 shows on the left side magnitude and phase plots of the accelerance frequency response functions (FRFs) for the uncontrolled system and the controlled system with different gain values. As the gain increases, the magnitudes around the resonance peaks decrease accordingly. Thus, as known from the literature [1], (direct) velocity feedback provides additional damping of the natural frequencies of the controlled system. To analyze the stability of the control system, a root locus plot is given in Fig. 4, where the poles are indicated by “x" markers and the zereos by “o" markers. Both poles and zeroes are complex conjugate pares, but throughout the paper only the positive half of the imaginary axes is shown for simplicity. Note the alternating poles and zeroes, a known effect of this type of control. Since no root locus enters the positive real part, it can be seen that the collocated configuration guarantees the stability of the control system for all gain values.

For the non-collocated case, also depicted in Fig. 2, the closed-loop transfer function reads

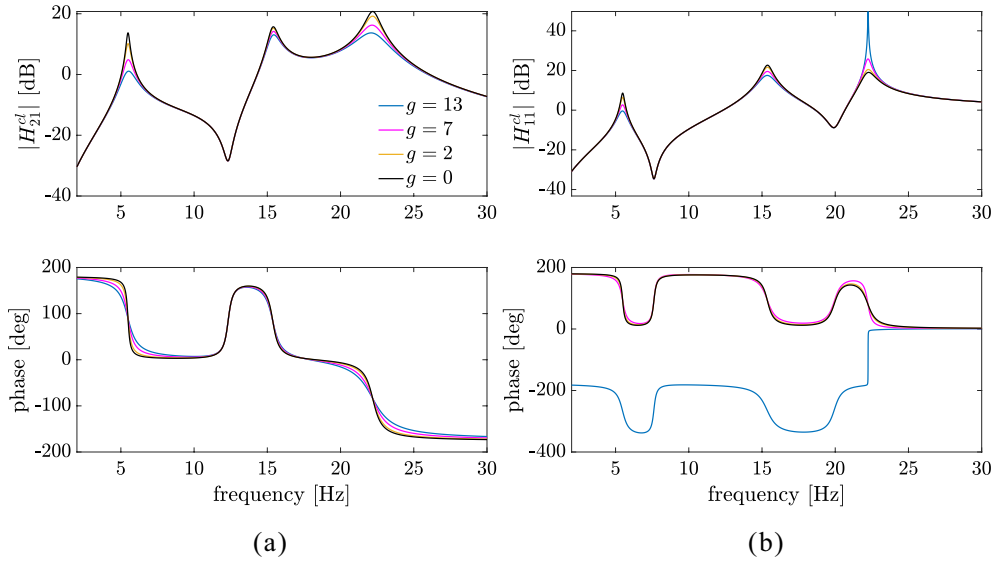

Fig. 3 Magnitude and phase plots of the accelerance FRF for: **a** collocated and **b** non-collocated configurations, where $g = 0$ corresponds to the uncontrolled case

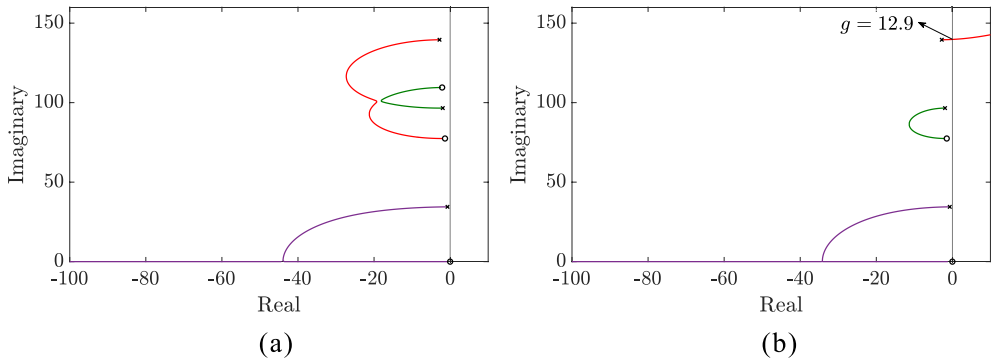

Fig. 4 Root locus for: **a** collocated and **b** non-collocated configurations

$$H_{11}^{cl}(s) = \frac{A_1(s)}{F_1(s)} = \frac{H_{11}(s)}{1 + G(s)H_{12}(s)} \tag{9}$$

In this case, the FRFs in Fig. 3 show that the non-collocated configuration can result in larger magnitudes around resonance peaks than the uncontrolled system. The root locus in Fig. 4 shows that a pole-zero flipping takes place [1]. Here, instability occurs in the controlled system for gain values higher than 12.9. Thus, a gain of 13 as seen in Fig. 3 represents unstable behavior.

2.4 Compensator for non-collocated control

The aim of the proposed compensator is to avoid instability of the control system for the non-collocated configuration, while mitigating vibration in a non-collocated setup by having only information about the uncontrolled system. To this end, a second-order compensator in the form of

$$H_c(s) = \frac{s^2 + 2\xi_z\omega_z s + \omega_z^2}{\omega_z^2} \tag{10}$$

is proposed. ω_z and ξ_z are the parameters to be assigned, representing a frequency and a damping ratio. Thus, the compensator introduces a pair of complex conjugated zeroes into the control system, providing a 180 ° phase lead. It is important to note that this is an improper transfer function, leading to unbounded behavior at high frequencies. Although in this idealized example the resulting control system is still proper, in real systems further measures must be taken to ensure stability, such as the use of filters. This is discussed in sect.3.3, where a low-pass filter of the same order as the used compensator is applied to address this amplification of the response.

When the transfer function of Eq. (10) is added to the feedback path, the denominator of the closed-loop transfer function in Eq. (9) becomes $1 + H_c(s)G(s)H_{12}(s)$. The frequency ω_z and damping ξ_z compensator parameters are obtained from a zero of the uncontrolled system. Figure 4 shows that the absence of a zero between the two poles leads to instability in the non-collocated case. In the frequency domain, these poles correspond to the second and third damped natural frequencies, while the zero corresponds to an anti-resonance between them. Therefore, ω_z and ξ_z are obtained directly from the anti-resonance in H_{22}, the transfer function used in the feedback path of the collocated control (compare with Fig. 2). These values are given in Table 1.

A schematic representation of the process of determining the compensator parameters is shown in Fig. 5. For a generic target point of vibration control at DoF p and a control applied at DoF q, the first step is to determine H_{pq}, where between the resonance peaks ω_n and ω_{n+1} the absence of an anti-resonance (or the absence of a zero in the pole-zero map) can be observed, resulting in a phase shift of 180 °. Then, the point FRF H_{qq} is measured so that the values of the frequency ω_{zn} and the damping ratio ξ_{zn} can be obtained from the anti-resonance between the poles ω_n and ω_{n+1}. Finally, the compensator is designed so that in Eq. (10) $\omega_z = \omega_{zn}$ and $\xi_z = \xi_{zn}$.

Figure 5 also shows the root locus plot for the controlled system with this compensated velocity feedback. With a generic gain g, it can be seen that the damping ratios for all resonance peaks are increased.

For the current example with $\omega_z/2\pi = \omega_{z2}/2\pi = 17.43$ Hz and $\xi_z = \xi_{z2} = 1.92$ %, Fig. 6 shows magnitude and phase as well as the root locus plots for the controlled system for the same gain values as shown in Figs 3 and 4. For a better visualization, the magnitude is shown in linear scale (compared to dB in Fig. 3). The root locus plot shows that the system is now unconditionally stable. Optimal performance in terms of vibration mitigation would be obtained for gain values corresponding to root loci with minimum real part, i.e. maximum damping. For the present example, this gain would be around 250, resulting in a more pronounced amplitude reduction.

2.5 Parametric study

By varying the parameters of the system to be controlled, the validity of the proposed compensator is investigated. Figure 7 depicts the FRFs for non-collocated control of the generic 3 DoF example, where

Table 1 Frequencies and damping ratios of resonances and anti-resonances of H_{22}

k	$\omega_k/2\pi$ [Hz]	ξ_k [%]	$\omega_{zk}/2\pi$ [Hz]	ξ_{zk} [%]
1	5.49	2.00	12.33	1.74
2	15.37	2.00	17.43	1.92
3	22.21	2.00	–	–

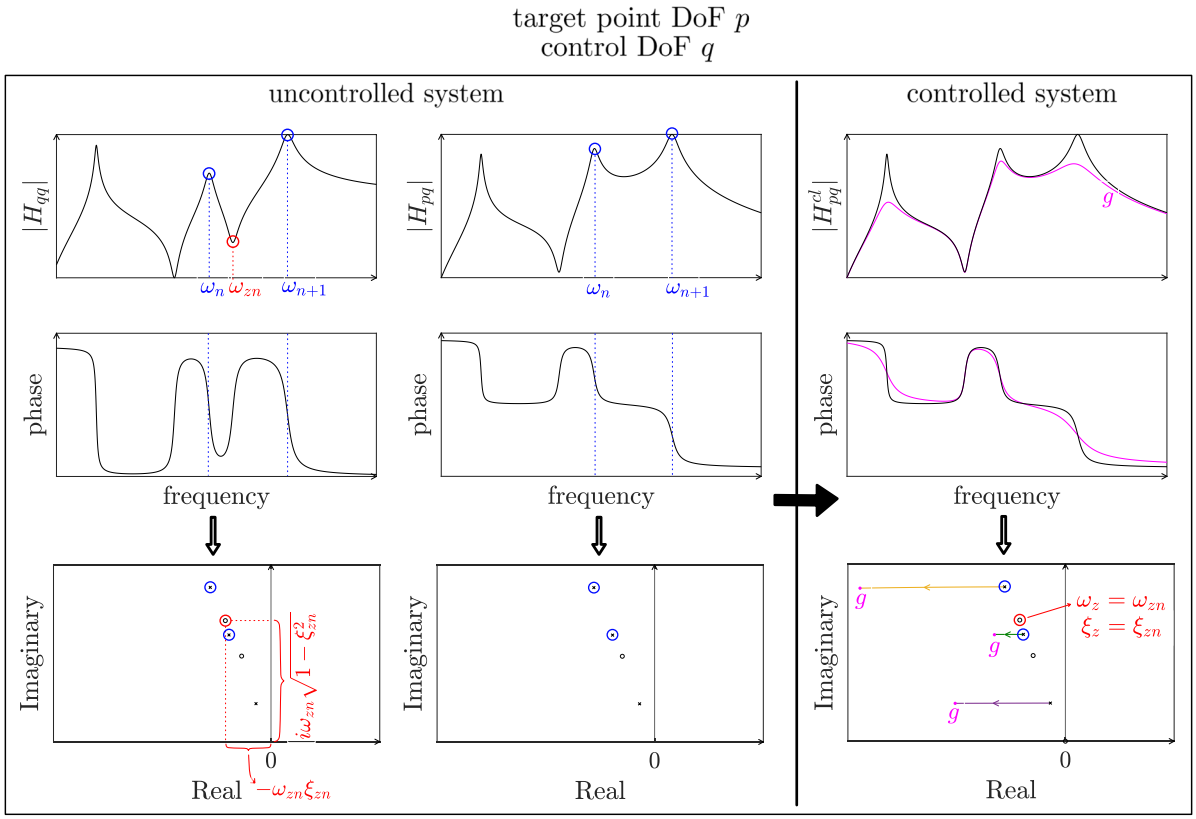

Fig. 5 Schematic representation of compensator parameter selection

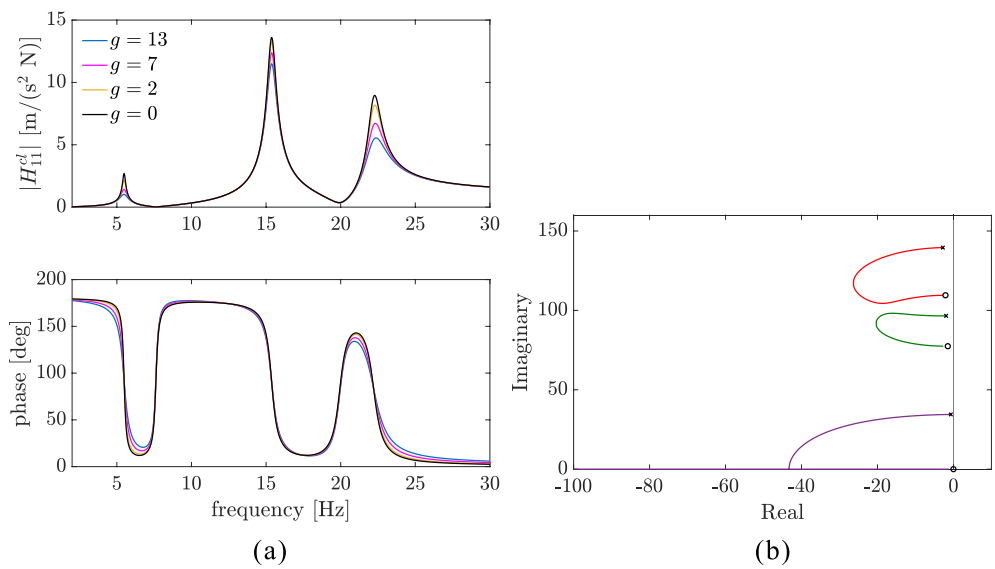

Fig. 6 Controlled system with $\omega_z/2\pi = 17.43$ Hz and $\xi_z = 1.92$ %, with **a** magnitude and phase plots of the accelerance FRF, where $g = 0$ corresponds to the uncontrolled case; **b** root locus plot

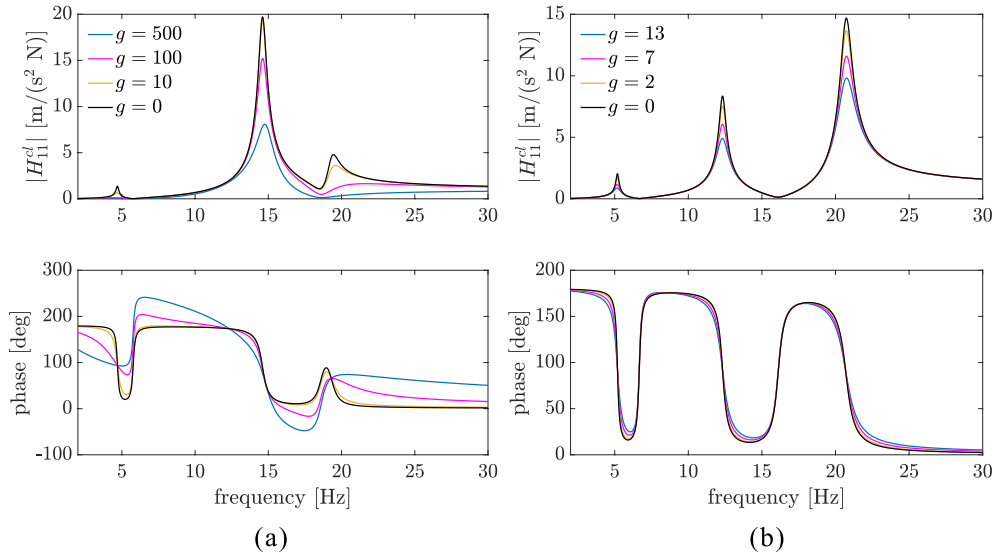

Fig. 7 Magnitude and phase plots of the accelerance FRF of the uncontrolled ($g = 0$) system and of the controlled systems for reduced spring stiffness: **a** $k_2 = 3000$ N/m and **b** $k_3 = 3000$ N/m

either spring stiffness k_2 or k_3 is reduced to 3000 N/m, i.e., one half of the other spring stiffness values. As a result, the poles and zeroes of the uncontrolled system change, such that for each case the zero of interest must be recalculated so that its frequency and damping ratio can be used for the compensator, as discussed in sect.2.4. For the first case considered with k_2 reduced, the response at DoF 1 is dominated by the second mode. In addition, modes 2 and 3 are more closely spaced than in the original setup. For gains in the order of magnitude as considered before, almost no amplitude reduction for the second resonance peak is observed, hence larger gains ($g = 100$ and 500, respectively) are considered in this case to highlight the control performance more clearly. In view of the practical implementation of the control law (considering the actuator dynamics and the influences of higher modes and noise), it is questionable whether such high gains can be realized. Therefore, limitations in the control performance for closely spaced modes can be expected. On the other hand, the reduction of k_3 distributes the natural frequencies of the system more evenly than in the original system such that the control performance is good for all three modes even for small gains.

A parametric study of the proposed compensator parameters can also be performed. For example, it is possible to completely suppress control for a desired resonance frequency by placing the zeroes exactly at the pole corresponding to the target frequency, a known effect for the assignment of transmission zeroes in control systems [23]. This case is given in Figs 8 and 9, where ω_z/ξ_z are chosen to coincide with ω_2/ξ_2 and ω_3/ξ_3, respectively (compare with Table 1). The figures show that the proposed compensator can be used to force the non-collocated control to behave almost as it was a collocated one, as seen through the root locus, except for the “spared mode". However, larger gains are required for the compensated system to achieve the same amount of damping as the collocated system.

In a real-world application of the proposed compensator, the system is more complex than the 3 DoF example analyzed. There are other elements such as out-of-band modes, filters, or the actuator dynamics that introduce additional poles and zeroes. The time delay may be a problem that limits the stability of the controlled system. Therefore, in the next step the proposed control is applied to a CLT panel which is excited by electrodynamic shakers.

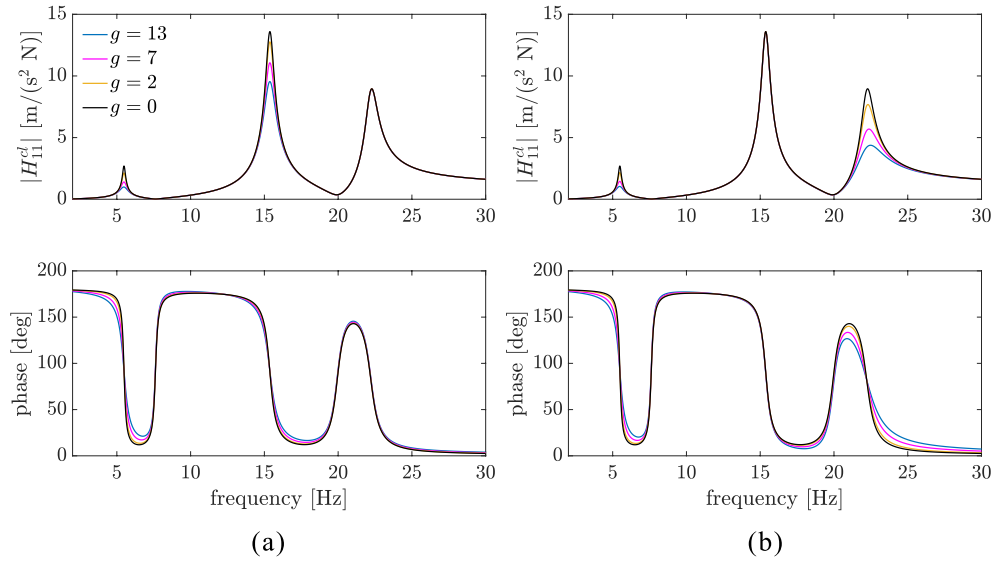

Fig. 8 Magnitude and phase plots of the accelerance FRF of the uncontrolled ($g = 0$) and of the controlled system with: **a** $\omega_z/2\pi = 22.21$ Hz, $\xi_z = 2.00$ % and **b** $\omega_z/2\pi = 15.37$ Hz, $\xi_z = 2.00$ %

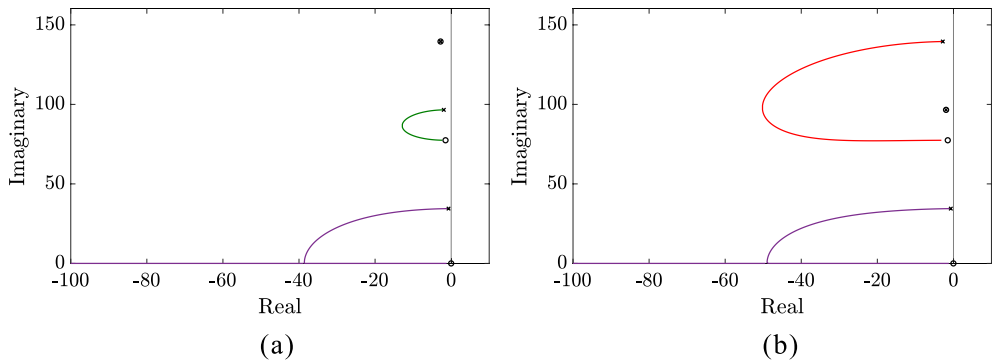

Fig. 9 Root locus of the controlled system with: **a** $\omega_z/2\pi = 22.21$ Hz, $\xi_z = 2.00$ % and **b** $\omega_z/2\pi = 15.37$ Hz, $\xi_z = 2.00$ %

3 Experimental verification

3.1 Experimental setup

Figure 10 shows the experimental setup tested in the laboratory of the Unit of Applied Mechanics at the Universität Innsbruck. It is composed of a three-layer CLT panel with dimensions 2 m × 0.975 m × 0.1 m and two electrodynamic shakers. To tune the natural frequencies of the panel to a range realistic for CLT floors, additional weights are added to the panel.

The CLT panel is fixed to a rigid table with two aluminum profiles at one of its corners (upper left corner in Fig. 10), and three Brüel&Kjaer 4508B accelerometers are placed at the remaining corners, which are numbered in the figure for easy reference. Two APS 400 Electro-Seis long-stroke shakers from APS Dynamics, Inc., are attached to the corners denoted as Accelerometer 1 and Accelerometer 2 and are fed by APS 145 power amplifiers. ME Meßsysteme KM26z force sensors are used to measure the input forces, while the input voltage and current to the shakers are provided from the power amplifier. Data acquisition is performed by a National Instruments CompactDAQ (NI cDAQ-9178) system. Control is provided by a National Instruments

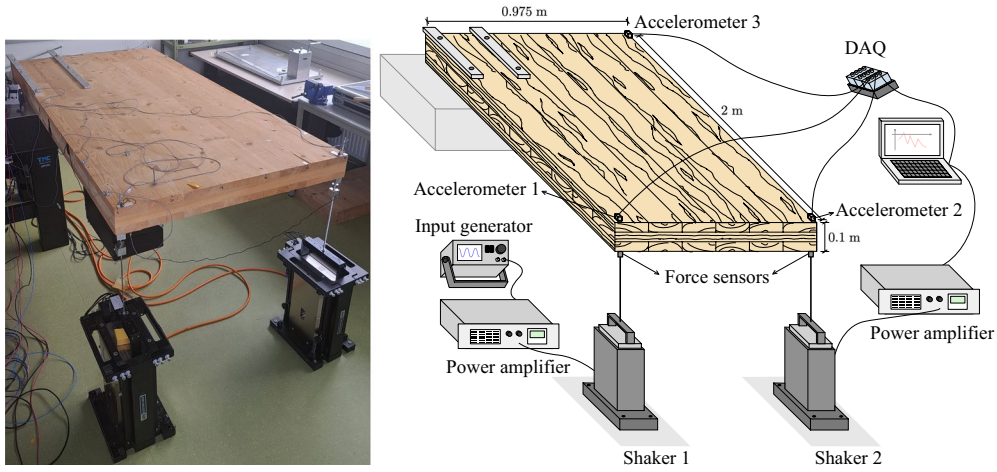

Fig. 10 **a** Photo and **b** illustration of the experimental setup

CompactRIO system (NI cRIO-9037) using another Brüel&Kjaer 4508B accelerometer as the measurement sensor. Both systems use National Instruments NI-9234 analog-digital-converter modules, which provide 24 bit precision at a maximum sampling rate of 25.6 kHz.

For the system identification discussed in sect.3.2, a multi-input multi-output (MIMO) system of the CLT-shaker assembly is considered, where both shakers excite the structure simultaneously. Two independent white noise signals with time period of 60 s and frequency range from 5 Hz to 45 Hz are used. Meanwhile, for the vibration control tests, shaker 1 provides white noise excitation in the same way, while shaker 2 serves as actuator for control.

It should be noted that the experimental setup is slightly nonlinear. This is due to the boundary conditions and the CLT panel itself. Specifically, the panel, which is fixed to a laboratory table, tends to lift off the table slightly at larger excitation amplitudes. On the other hand, cracks and gaps between the boards of the CLT panel open and close during vibrations, hence a slight decrease in stiffness (i.e. natural frequencies) and an increase in damping of the slab is to be expected as the excitation amplitudes increase. This must be taken into account when comparing the results from the uncontrolled and the controlled systems, where the vibration response for the latter is smaller for the same excitation level.

3.2 Uncontrolled system

In this section, an electromechanical model of the experimental CLT panel-shaker setup is developed to compare experimental and simulation data in the following sections. The CLT panel is assumed to be a linear, time-invariant system that can be described by equations of motion in the same form as the generic 3 DoF system discussed in sect.2.1, Eq. (1). Here $\mathbf{x}(t) = [x_1(t)\ \ x_2(t)\ \ x_3(t)]^T$ is the response vector measured at the three corners depicted in Fig. 10, while $\mathbf{f}(t) = [f_{S1}(t)\ \ f_{S2}(t)\ \ 0]^T$ is the vector of external forces provided by the shakers. For the frequency range of interest specified in sect.3.1, three natural frequencies are present. Therefore, a modal truncation can be implemented for $n = 3$ to write the equations of motion in terms of modal coordinates using the same relation as in Eq. (2), yielding three modal equations of motion in the same form as in Eq. (4). The only difference is that there are now two input forces on the right-hand side.

Each of the two electrodynamic shakers shown in Fig. 11 consists of a body, which is assumed to be rigidly attached to the ground, and a moving mass m_{Si} with degree-of-freedom $x_{Si}(t)$, which is coupled to the body by a spring-damper element (spring stiffness k_{Si}, damping coefficient b_{Si}). The subscript S stands for "shaker" and $i = 1, 2$. An electric current in a coil generates the Lorentz force $f_{Si}^c(t) = \alpha_i \dot{q}_i(t)$, which

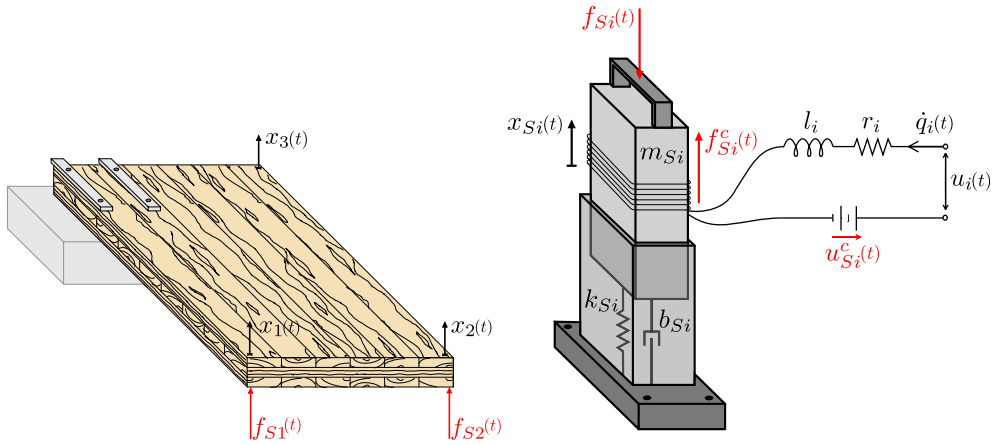

Fig. 11 Schematic representations of: **a** CLT panel and **b** electrodynamic shaker

drives the moving mass, where $\dot{q}_i(t) = i(t)$ is the current, $q_i(t)$ is the charge, and α_i is the force-to-current ratio. The shaker is driven by a voltage $u_i(t)$ through the power amplifiers. The equivalent electrical circuit can be described by an inductance l_i, a resistance r_i and a voltage induced by the moving magnetic field, given by $u^c_{Si}(t) = \beta_i \dot{x}_{Si}(t)$ with a coupling factor β_i [36]. While in an ideal electrodynamic actuator, $\alpha_i = \beta_i$ would hold, here two separate coupling factors are used to better represent experimental results, considering that the present electromechanical shaker model is a simplification. Thus, each shaker can be described by two coupled equations of motion in terms of degrees-of-freedom $x_{Si}(t)$ and $q_i(t)$ as

$$\begin{cases} \ddot{x}_{Si}(t) + 2\xi_{Si}\omega_{Si}\dot{x}_{Si}(t) + \omega^2_{Si}x_{Si}(t) &= \dfrac{1}{m_{Si}}\left(\alpha_i\dot{q}_i(t) - f_{Si}(t)\right) \\ l_i\ddot{q}_i(t) + r_i\dot{q}_i(t) + \beta_i\dot{x}_{Si}(t) &= u_i(t) \end{cases} \tag{11}$$

where $\omega^2_{Si} = k_{Si}/m_{Si}$ is the natural frequency and $\xi_{Si} = b_{Si}/(2m_{Si}\omega_{Si})$ is the damping ratio of the mass-spring-damper assembly.

Coupling of the CLT and shaker subsystems is accomplished via the forces $f_{Si}(t)$ and assuming that the displacement of each shaker is equal to the displacement of the panel at each position $\left(x_{Si}(t) \equiv x_i(t)\right)$. Employing the modal coordinates as in Eq. (2) for the panel, the coupling forces are obtained from the first equation in Eq. (11) as $f_{Si}(t) = \alpha_i\dot{q}_i(t) - m_{Si}\sum_{k=1}^{3}\left[\phi_{ki}\ddot{y}_k(t) + 2\xi_{Si}\omega_{Si}\phi_{ki}\dot{y}_k(t) + \omega^2_{Si}\phi_{ki}y_k(t)\right],\ i = 1, 2$. The complete dynamics of the CLT-shakers system is then given by five coupled differential equations,

$$\begin{cases} \ddot{y}_k(t) + 2\xi_k\omega_k\dot{y}_k(t) + \omega^2_k y_k(t) &= \dfrac{1}{\tilde{m}_k}\left(\phi_{k1}\,f_{S1}(t) + \phi_{k2}\,f_{S2}(t)\right), \quad k = 1, 2, 3 \\ l_i\ddot{q}_i(t) + r_i\dot{q}_i(t) + \beta_i\left(\displaystyle\sum_{k=1}^{3}\phi_{kn}\dot{y}_k(t)\right) &= u_i(t), \quad i = 1, 2 \end{cases} \tag{12}$$

Note that the inputs to the coupled system are not given by the forces applied to the plate, but rather by the voltages $u_1(t)$ and $u_2(t)$ supplied to each shaker. Using the Laplace transform of Eqs 12, transfer functions can be derived and evaluated at $s = i\omega$, yielding FRFs that are compared to experimental data. In what follows, H_{1i}, H_{2i}, H_{3i} correspond to the FRFs for the accelerations in each corner of the slab and H_{4i}, H_{5i}

to the FRFs for currents $\dot{q}_1(t), \dot{q}_2(t)$ in the shaker coils, respectively, due to input voltage u_i, $i = 1, 2$. In Figs 12 and 13 experimental results for these FRFs are shown with dots. Three natural frequencies can be identified in the frequency range from 10 to 30 Hz, where the first two are closely spaced.

The experimental data are contrasted with the outcomes obtained using the derived electromechanical system, which shows a very accurate match, except for a slight deviation in the phase plots for the currents at the respective driving points (H_{41} and H_{52}). The system properties were obtained by solving an optimization problem employing the simplex algorithm implemented in the Matlab *fminsearch* function [37]. The masses of the shakers were assumed to be equal to $m_{Si} = 2.7$ kg (as given in the data sheet) and the modal coefficients ϕ_{k1} were set to unity. The 27 remaining parameters of the model, i.e. natural frequencies ω_k, damping ratios ξ_k, modal masses $\tilde{m}_k$, mode shape coefficients ϕ_{k2} and ϕ_{k3}, inductances l_i, resistances r_i, shakers natural frequencies ω_{Si} and damping ratios ξ_{Si}, and coupling factors α_i and β_i were optimized to minimize the sum of the mean squared error between the model and experimental FRF magnitude and phase curves in the frequency range from 10 to 30 Hz, using all of the ten FRFs shown above. Tables 2 and 3 show the optimized parameters of both the shakers and the CLT panel.

Figures 12 and 13 show the magnitude and phase plots of the accelerance FRF for the experimental data and the model with the obtained parameters. It can be seen that the phase plots of the model with respect to H_{41} and H_{52} have a deviation from the experimental data. This may be due to nonlinearities in the circuits of the real system that were not considered in the model. Furthermore, differences between the curves can also be explained by the influence of higher vibration modes not considered in the model.

For a better visual representation of the three modes of the panel, results from a previous experimental modal analysis (EMA) using a denser measurement grid are shown in Fig. 14, obtained in a experiment performed six months before the other results in the present paper. Accordingly, modes 1 and 2 are bending dominated modes of the panel, while mode 3 is a primarily torsional mode. The modal parameters given in Table 4 were obtained using the LSCE algorithm [32, 38] as implemented in the Matlab function *modalfit* on this data. A comparison with the values given in Table 3 reveals small deviations. This is most likely due to the nonlinearity of the CLT panel mentioned above and the fact that the EMA was performed approximately six months earlier. During this period, the internal structure of the CLT panel changed (i.e., moisture content and mass due to external moisture changes and possibly creep-induced cracks), highlighting the challenges of obtaining accurate model parameters for what appears to be a relatively simple structure.

Table 2 Parameters of the shakers

i	m_{Si} [kg]	l_i [H]	r_i [Ω]	$\omega_{Si}/2\pi$ [Hz]	ξ_{Si} [%]	α_i [N/A]	β_i [V s/m]
1	2.7	0.0195	1.712	1.48	44.9	17.719	19.616
2	2.7	0.0200	1.778	1.20	37.9	18.615	20.318

Table 3 Parameters of the CLT panel

k	$\omega_k/2\pi$ [Hz]	ξ_k [%]	$\tilde{m}_k$ [−]	ϕ_{k1} [−]	ϕ_{k2} [−]	ϕ_{k3} [−]
1	15.19	2.00	36.4	1	1.172	-0.252
2	18.53	1.86	165.6	1	-1.984	-2.335
3	27.33	1.68	41.9	1	-1.687	0.949

Table 4 Parameters of the CLT panel obtained from previous experimental modal analysis

k	$\omega_k/2\pi$ [Hz]	ξ_k [%]	$\tilde{m}_k$ [−]	ϕ_{k1} [−]	ϕ_{k2} [−]	ϕ_{k3} [−]
1	15.46	1.60	50.3	1	1.071	−0.312
2	18.30	2.12	229.6	1	-2.652	−2.545
3	27.34	1.52	48.2	1	-1.590	0.951

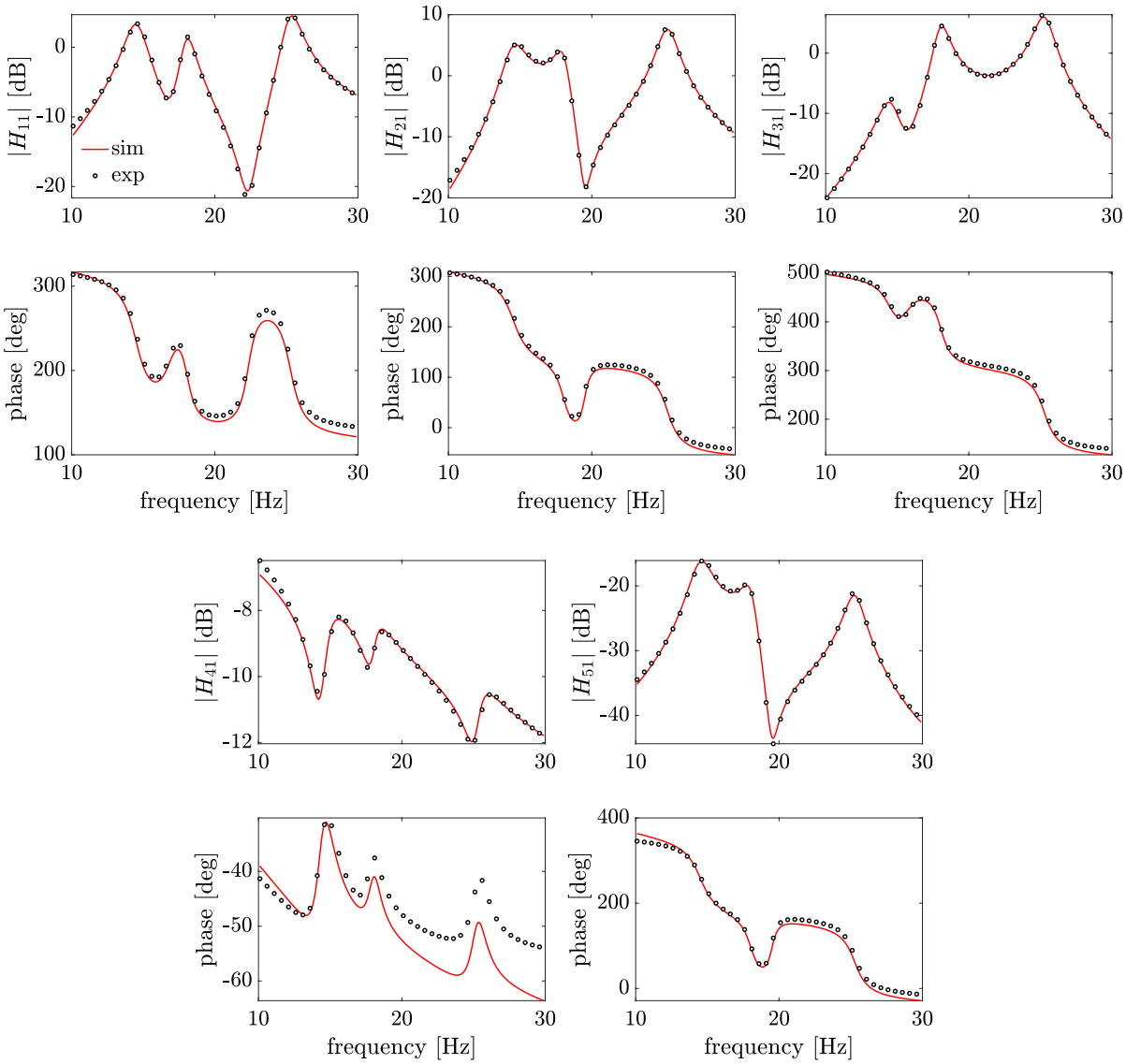

Fig. 12 Magnitude and phase plots of the coupled CLT-shakers system for input voltage u_1 with simulation results of the model (sim) and results from experiments (exp)

3.3 Components of the controlled system

Compared to the ideal compensator introduced in sect.2.4, in a real-world application additional components must be considered in the feedback path, as shown in the block diagram in Fig. 15. These include a high-pass and low-pass filters, power amplifier dynamics, a voltage saturation, and possible delay, represented by transfer functions.

Since the ideal integrator block $1/s$ to compute velocities from the measured acceleration A_1 amplifies low-frequency noise, a high-pass filter is applied. A second-order Butterworth filter is used [39], described by a transfer function of the form $H_{hp}(s) = s^2/\left(s^2 + \sqrt{2}\,\omega_{hp}s + \omega_{hp}^2\right)$, where the cut-off frequency is $\omega_{hp}/2\pi = 7$ Hz. Similarly, the ideal compensator H_c, as given by the transfer function Eq. (10), amplifies the high-frequency noise such that

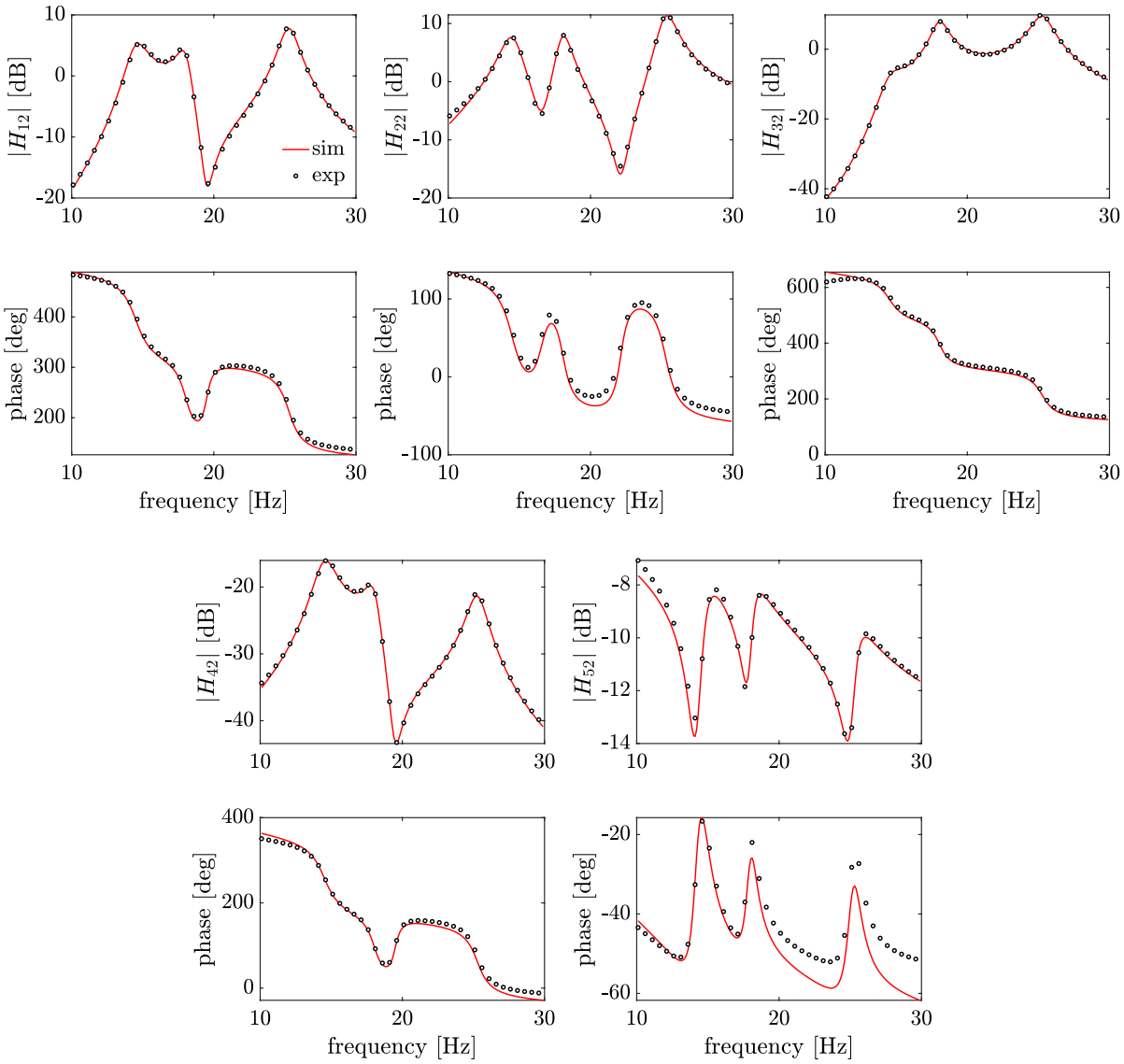

Fig. 13 Magnitude and phase plots of the coupled CLT-shakers system for input voltage u_2 with simulation results of the model (sim) and results from experiments (exp)

a low-pass filter is used. Again, a second-order Butterworth filter [39] $H_{lp}(s) = \omega_{lp}^2 / \left(s^2 + \sqrt{2}\,\omega_{lp} s + \omega_{lp}^2\right)$ is used, with cut-off frequency $\omega_{lp}/2\pi = 170$ Hz.

Since the computed output voltage of the compensated velocity feedback controller may exceed the input range of the power amplifiers and/or the analog output module used in the controller, a saturation of the output voltage is taken into account, in this case to ±5 V. Previous experiments have shown that the voltage input–output characteristics of the power amplifiers used are not ideal, but an additional first-order high-pass filter is implemented to limit the capabilities in the very low frequency range. The corresponding amplifier transfer function [39] was obtained as $H_{amp}(s) = g_a s / \left(s + \omega_a\right)$, with amplifier gain $g_a = 18.4$ and cut-off frequency $\omega_a/2\pi = 1.65$ Hz. Finally, the analog-digital converter modules used introduce a non-negligible amount of time delay (latency), although they

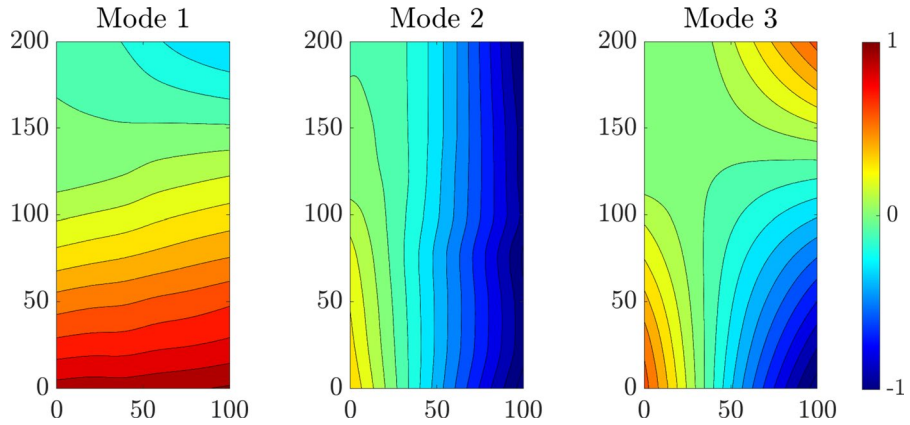

Fig. 14 Vibration modes of the CLT panel with modal parameters as in Table 4

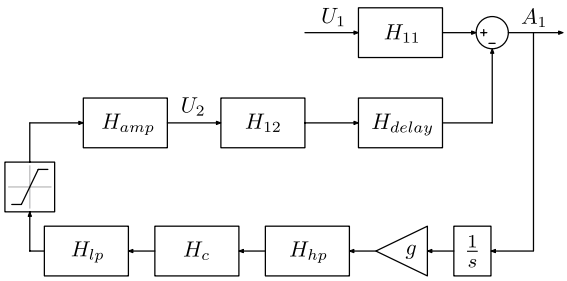

Fig. 15 Block diagram for non-collocated control of the CLT panel

are accurate and capable of high sampling rates. According to the data sheet, the delay is about $40/f_s$, where f_s is the sampling rate. For $f_s = 25.6$ kHz, this would result in a delay of $\tau = 1.5$ ms. By analyzing the experimental data, a value of $\tau = 1.0$ ms was obtained for the implemented system. The transfer function of a pure time delay is $H_{delay}(s) = e^{-s\tau}$, which is approximated for simulation purposes by the Padé approximation $H_{delay}(s) = (1 - s\tau/2)/(1 + s\tau/2)$.

Figure 16 shows the magnitude and phase plots of the FRFs for the compensator and different combinations of elements that make up the feedback path, so that the influence of each element in the control

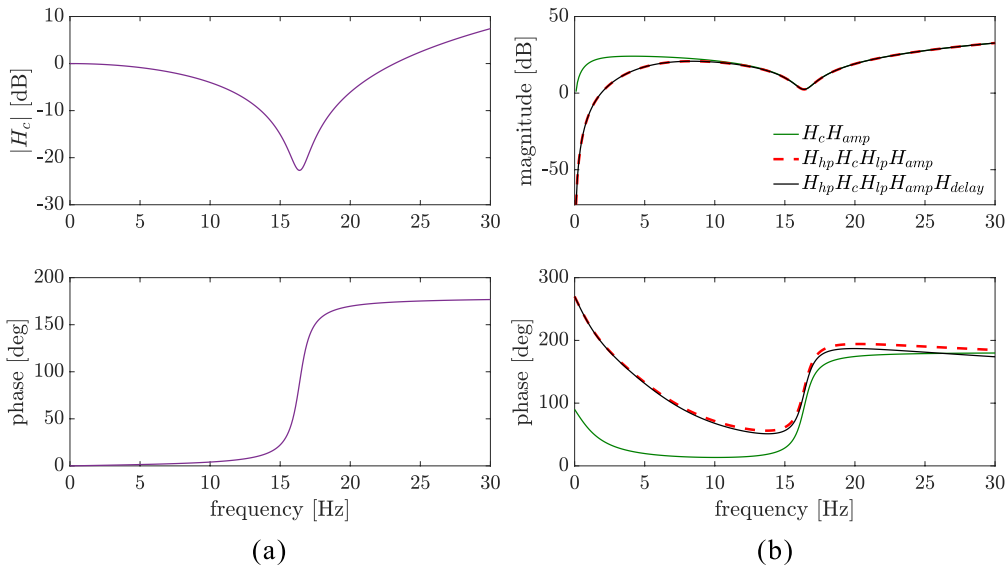

Fig. 16 Magnitude and phase plots of: **a** compensator; **b** different combinations of elements in the feedback path

system can be analyzed individually. The compensator contributes not only with a drop in amplitude around the selected frequency, but also with a phase lead that tends to 180 °. This is the expected effect of introducing a pair of complex conjugate zeros, as discussed in sect.2.1. The same figure also shows that the amplifier has an effect (other than shifting magnitudes to higher values) only at lower frequencies. The effect of the high pass filter is visible in both the magnitude and phase plots, while the low pass filter does not change the behavior of the system in the frequency range considered. However, as mentioned earlier, it provides stability with respect to higher frequency noise. Furthermore, the presence of a time delay with $\tau = 1.0$ ms in the control system is visible in the phase response above about 20 Hz.

It should be emphasized that the actual transfer function implemented on the controller hardware using LabView Realtime is the time-discrete version of $H_{ctrl}(s) = g(1/s)H_c(s)H_{hp}(s)H_{lp}(s)$ and the saturation block, while all other transfer functions depicted in Fig. 15 are used for simulation purposes only. Here, the saturation is neglected to keep the simulation model linear. Thus, the controller does not rely on a plant model of the system to be controlled, although for a proper anti-resonance assignment of the parameters ω_z and ξ_z, prior testing of the uncontrolled system is obvious.

3.4 Controlled system

This section presents the comparison of simulation and measurement data of the controlled system for the non-collocated velocity feedback control with the proposed compensator as shown in Fig. 15. Specifically, shaker 1 provides excitation to the panel via voltage U_1 at Accelerometer 1 (compare with Fig. 10). The vibration response at this corner is controlled, i.e. using accelerations A_1, by shaker 2 (voltage U_2) located at Accelerometer 2. Since the transfer function H_{12} of the uncontrolled system introduces additional 180 ° phase lag between the first and second natural frequency (see Fig. 13), the relevant anti-resonance for the compensator H_c is taken from the transfer function H_{22} between these two natural frequencies. From Fig. 13, the zeroes $z = -3.77 \pm 103i$ are obtained, yielding the parameters $\omega_z/2\pi = 16.4$ Hz and $\xi_z = 3.66$ %.

Figure 17 shows magnitude and phase plots of the corresponding closed-loop transfer function H_{11} employing these parameters for this compensated velocity feedback (CVF). A very good approximation of the experimental data by the simulation can be observed. Compared to the uncontrolled system, all three resonance peaks are reduced, verifying the proposed controller. However, as already observed in the generic 3 DoF example in sect.2.1, the control performance is limited for the present situation with

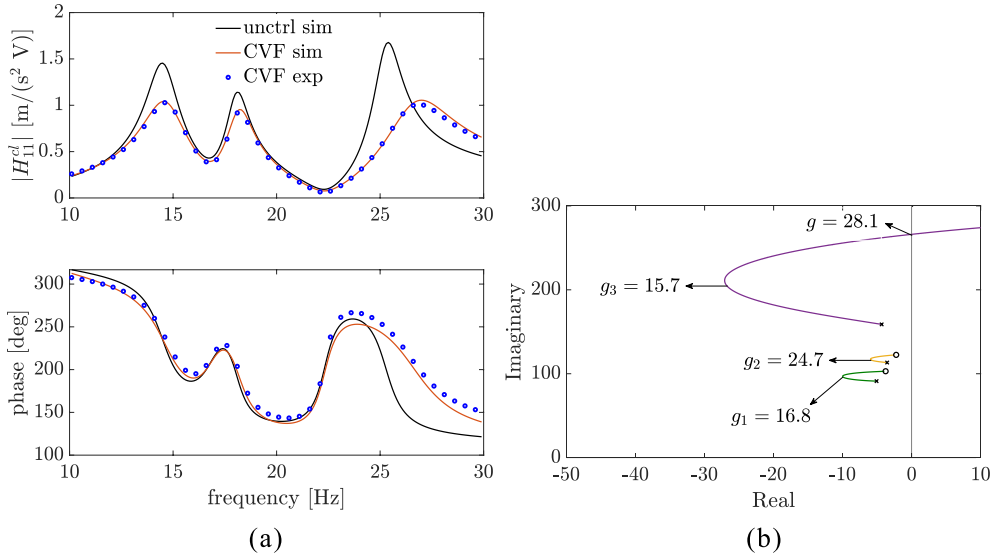

Fig. 17 Uncontrolled (unctrl) and controlled (CVF) systems for compensator parameters $w_z/2\pi = 16.4$ Hz and $\xi_z = 3.66$ %, gain $g = 5$ V/ms^{-2}, with **a** magnitude and phase plots; **b** root locus plot

closely spaced modes. In the experimental test, instability occurred for gains higher than $g = 5$ V/ms^{-2}. The root locus plot of the simulation model in Fig. 17 (limited to the three structural roots) suggests that the third root/natural frequency is responsible for this instability, but for higher gains $g > 28.1$ V/ms^{-2}. This discrepancy can be explained by the fact that in the actual test higher modes are not captured by the three-mode simulation model with introduce instability. Further experimental tests revealed that the fourth and fifth natural frequency of the plate are around 85.1 and 102 Hz, respectively.

The influence of time delay can also be explored. Since this is embedded to the real setup of the control system, it can only be achieved by simulation. Figure 18 depicts this ideal situation with the same experimental results as in Fig. 17 and the same parameters in the simulation, but now without delay. The presence of the time delay results in higher amplitudes around the third resonance peak.

Further investigation of the effects of the filters in the control system is also possible. Figure 19 shows experimental and numerical results for different combinations of cut-off frequencies of both low-pass and high-pass filters for the same compensator

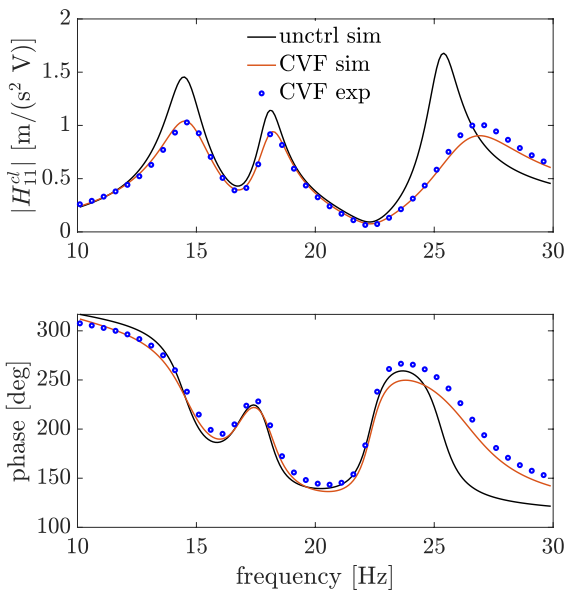

Fig. 18 Magnitude and phase plots of the uncontrolled (unctrl) and controlled (CVF) systems without delay for compensator parameters $w_z/2\pi = 16.4$ Hz and $\xi_z = 3.66$ %, gain $g = 5$ V/ms^{-2}

parameters. By lowering the value of ω_{lp}, a higher gain $g = 7$ V/ms^{-2} could be used before instability. Slightly lower amplitudes around the first resonance frequency can be seen, but at the cost of larger amplitudes for the third resonance peak. The figure also shows that higher values of ω_{hp} result in slightly higher amplitudes around the first resonance peak and a reduction of amplitudes in the frequency range after it. A noticeable discrepancy between experimental data and simulation can be seen for the case $\omega_{lp}/2\pi = 100$ Hz and $\omega_{hp}/2\pi = 3$ Hz. Later experimental results considering higher vibration modes showed that this is due to their influence.

Based on the simulation model, the sensitivity of the compensator parameters ω_z and ξ_z on the control performance can be investigated. By varying these parameters, from the simulated closed-loop FRF a performance index in the form of

$$J = \int_{\omega} \left[H_{11}^{cl}(\omega)\right]^2 \, \mathrm{d}\omega \tag{13}$$

is computed in the frequency range from 10 to 30 Hz. Figure 20 shows a contour plot of this performance index with corresponding gains for each pair of parameters.

The plot was created as follows: take, for example, the pair $w_z/2\pi = 16.4$ Hz and $\xi_z = 3.66$ %, shown in the same figure by a red dot, corresponding to the results in Fig. 17. g_1, g_2, g_3 are the gains where maximum damping is achieved for each pole. The gain used in the performance index corresponds to the lowest value between them, in this case $g_3 = 15.7$ V/ms^{-2}. Since the goal here is to reduce all three resonance peaks, the cases where no additional damping is introduced by the control for one of the first two poles of the closed loop are not considered, corresponding to the blank space in Fig. 20. Furthermore, to account for instability, the cases where instability occurs for one of these first two poles are also not considered and are also represented by the blank spaces. It can be observed that within a frequency range of $16.2\,\text{Hz} < \omega_z/2\pi < 17.5\,\text{Hz}$ and $2.9\,\% < \xi_z < 6.6\,\%$ the performance is optimal, i.e. the compensator is relatively robust with respect to the exact determination of its parameters. However, as soon as ξ_z falls below a critical value, the performance index increases drastically, i.e. the control performance drops.

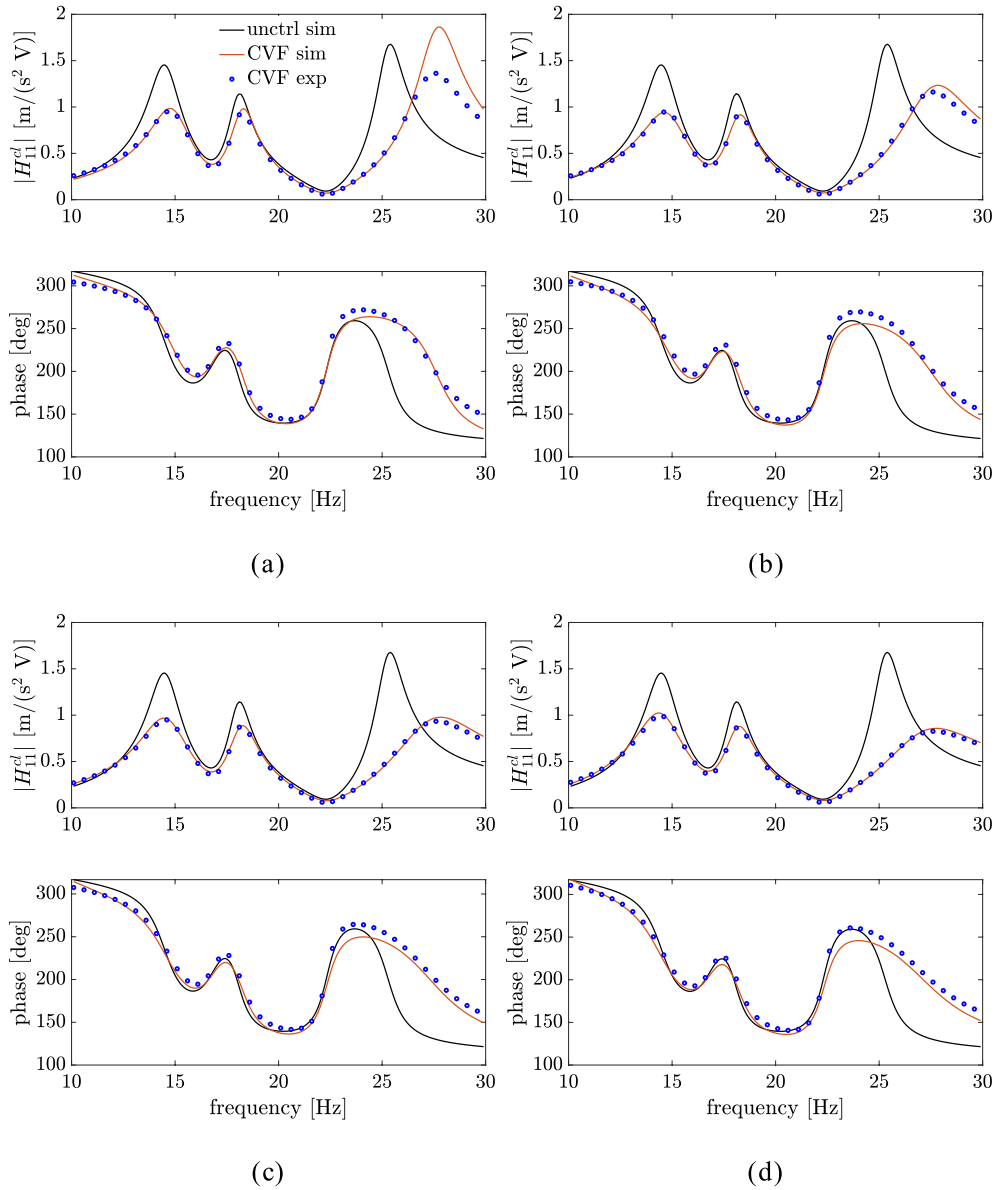

Fig. 19 Magnitude and phase plots of the uncontrolled (unctrl) and controlled (CVF) systems for compensator parameters $w_z/2\pi = 16.4$ Hz and $\xi_z = 3.66$ %, gain $g = 7$ V/ms^{-2} and the following parameters: **a** $\omega_{lp}/2\pi = 100$ Hz and $\omega_{hp}/2\pi = 3$ Hz; **b** $\omega_{lp}/2\pi = 100$ Hz and $\omega_{hp}/2\pi = 7$ Hz; **c** $\omega_{lp}/2\pi = 100$ Hz and $\omega_{hp}/2\pi = 10$ Hz; **d** $\omega_{lp}/2\pi = 100$ Hz and $\omega_{hp}/2\pi = 12$ Hz

4 Conclusions

A new compensator for non-collocated active vibration control based on velocity feedback was proposed. To account for the 180 ° phase lag present in such systems, which causes instability in conventional direct velocity feedback, a second-order compensator with two parameters (frequency and damping ratio) was used. Employing anti-resonance assignment, these parameters are taken from experimentally obtained anti-resonance information of the uncontrolled system. Apart from this (usually readily available) experimental data, no model of the plant is needed to implement the controller, unlike other control approaches such as optimal control. Hence, the

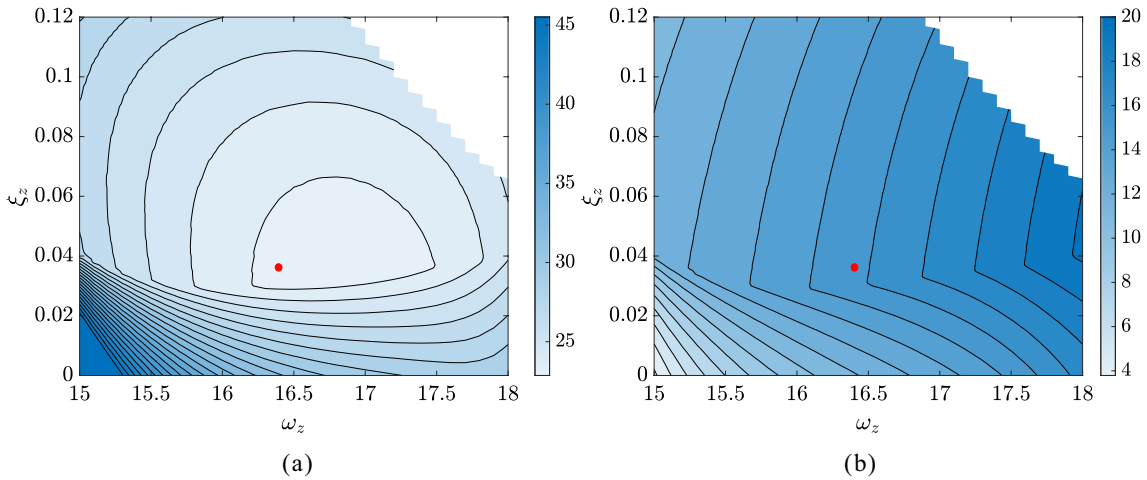

Fig. 20 **a** Control performance map and **b** the respective gain values used at each pair of compensator parameters ω_z and ξ_z, where the red dot corresponds to the proposed pair $w_z/2\pi = 16.4$ Hz and $\xi_z = 3.66$ %

controller is readily applicable even to slightly nonlinear models, which are often encountered in practice.

To this end, tests were performed on a cross-laminated timber panel in a frequency range where three natural frequencies dominate the dynamic response. Although the setup was relatively simple, a realistic scenario was obtained with relatively closely spaced natural frequencies in the range from 15 to 27 Hz with mild nonlinearities introduced by the boundary conditions and the nature of the CLT panel itself. A simple yet accurate linear electromechanical model of the system with three vibration modes of the panel and two electrodynamic shakers (one providing excitation, the other serving as actuator) was derived. This model can be easily adapted to other systems once the modal data and model parameters of the actuator are known.

The robustness of the control performance with respect to the two compensator parameters was investigated by numerical simulations, which showed a relatively low sensitivity of the parameters, except in the case where very small damping ratios are used in the compensator model. In these cases, the instability was more easily triggered.

For the practical implementation of the controller, both a high-pass and a low-pass filter were applied to counteract the effect of low and high frequency noise. Their influence on the control performance was evaluated both experimentally and through the model. Using second-order Butterworth filters, the phase-lag effect of the low-pass filter in particular should not be underestimated, even when the cut-off frequency is set to three to four times the highest considered natural frequency of the system.

In the experimental results, the effects of the time delay caused by the latency of the analog-digital converter were revealed and verified by the numerical model. In the present case, a delay of 1 ms caused a considerable performance loss for the third natural frequency at 27 Hz. To compensate this effect, additional compensators (as widely proposed in the literature) could be added.

In the present investigations, only cases with one 180° phase lag in the frequency range of interest (i.e. one “missing" anti-resonance) were considered. However, the proposed compensator is relatively easily extended for cases where more than one anti-resonance is to be placed. For example, using two second-order compensators increases the order of the transfer function to be implemented on the hardware by at least four, since the filter orders must be increased accordingly. Future studies should address the question of whether in this case two separately assigned anti-resonances influence each other in such a way that the compensator parameters can no longer be derived directly from the uncontrolled system data.

Author Contributions All authors contributed to the study conception and design. All authors read and approved the final manuscript.

Funding Open access funding provided by University of Innsbruck and Medical University of Innsbruck. This project ("Good Vibrations") has received funding from The Austrian Research Promotion Agency (FFG), Bridge program, under the FFG project number FO999891097.

Data availability The authors confirm that the data supporting the findings of this study are available within the article or are available from the corresponding author on request.

Declarations

Conflict of interest The authors declare that they have no Conflict of interest.

References

1. Preumont A (2018) Vibration Control of Active Structures: An Introduction. Springer, Cham
2. Meirovitch L (1990) Dynamics and Control of Structures. Wiley, United States of America
3. Ogata K (2010) Modern Control Engineering, 5th edn. Prentice Hall, New Jersey
4. Pérez-Aracil J, Pereira E, Díaz IM, Reynolds P (2021) Passive and active vibration isolation under isolator-structure interaction: application to vertical excitations. Meccanica 56:1921–1935. https://doi.org/10.1007/s11012-021-01342-2
5. Zenz G, Berger W, Gerstmayr J, Nader M, Krommer M (2013) Design of piezoelectric transducer arrays for passive and active modal control of thin plates. Smart Struct Syst 12:547–577. https://doi.org/10.12989/sss.2013.12.5.547
6. Masnata C, Pirrotta A (2024) Optimal design of inerter-based absorbers with amplified inertance: From the improved tuned liquid column damper inerter (ITLCDI) to the improved tuned mass damper inerter (ITMDI) and improved tuned inerter damper (ITID). Meccanica. https://doi.org/10.1007/s11012-024-01834-x
7. Schoeftner J, Krommer M (2012) Single point vibration control for a passive piezoelectric bernoulli-euler beam subjected to spatially varying harmonic loads. Acta Mech 223:1983–1998. https://doi.org/10.1007/s00707-012-0686-0
8. Baader J, Fontana M (2017) Active vibration control of lightweight floor systems. Procedia Eng 199:2772–2777. https://doi.org/10.1016/j.proeng.2017.09.529
9. Díaz IM, Reynolds P (2010) Acceleration feedback control of human-induced floor vibrations. Eng Struct 32:163–173. https://doi.org/10.1016/j.engstruct.2009.09.003
10. Gattringer H, Nader M, Krommer M, Irschik H (2003) Collocative PD control of circular plates with shaped piezoelectric actuators sensors. J Vib Control 9:965–982. https://doi.org/10.1177/107754603030576
11. Pereira BSS, Santos TLM, Araújo JM (2024) Receptance-based model predictive control of multibody systems with time-varying references. Meccanica 59:33–48. https://doi.org/10.1007/s11012-023-01737-3
12. Meng H, Sun X, Xu J, Wang F (2021) Multimodal vibration suppression of nonlinear Euler-Bernoulli beam by multiple time-delayed vibration absorbers. Meccanica 56:2429–2449. https://doi.org/10.1007/s11012-021-01384-6
13. Saldanha A, Silm H, Michiels W, Vyhlídal T (2022) An optimization-based algorithm for simultaneous shaping of poles and zeros for non-collocated vibration suppression. IFAC-PapersOnLine 55:394–399. https://doi.org/10.1016/j.ifacol.2022.09.056
14. Kim SM, Oh JE (2013) A modal filter approach to non-collocated vibration control of structures. J Sound Vib 332:2207–2221. https://doi.org/10.1016/j.jsv.2012.12.002
15. Hanagan LM, Murray TM (1997) Active control approach for reducing floor vibrations. J Struct Eng 123(11):1497–1505. https://doi.org/10.1061/(ASCE)0733-9445(1997)123:11(1497)
16. Shahabpoor, E., Reynolds, P., Nyawako, D.: A comparison of direct velocity, direct, and compensated acceleration feedback control systems in mitigation of low-frequency floor vibrations. In: Dynamics of Civil Structures, Volume 4, pp. 177–187. Springer, Jacksonville, Florida, USA (2011). https://doi.org/10.1007/978-1-4419-9831-6_19
17. Alujević N, Senjanović I, Ćatipović I, Vladimir N (2019) The absence of reciprocity in active structures using direct velocity feedback. J Sound Vib 438:251–256. https://doi.org/10.1016/j.jsv.2018.09.035
18. Kluever CA (2015) Dynamic Systems: Modeling, Simulation, and Control. Wiley, United States of America
19. Jamshidi R, Collette C (2022) Optimal negative derivative feedback controller design for collocated systems based on H_2 and H_∞ methods. Mech Syst Signal Process. https://doi.org/10.1016/j.ymssp.2022.109497
20. Mastory CG, Chalhoub NG (2016) Enhanced structural controllers for non-collocated systems. J Vib Control 22:678–694. https://doi.org/10.1177/1077546314530418
21. Ferrari G, Amabili M (2015) Active vibration control of a sandwich plate by non-collocated positive position feedback. J Sound Vib 342:44–56. https://doi.org/10.1016/j.jsv.2014.12.019
22. Shin C, Hong C, Jeong WB (2013) Active vibration control of beams using filtered-velocity feedback controllers

with moment pair actuators. J Sound Vib 332:2910–2922. https://doi.org/10.1016/j.jsv.2012.12.037
23. Mottershead JE, Tehrani MG, James S, Ram YM (2008) Active vibration suppression by pole-zero placement using measured receptances. J Sound Vib 311:1391–1408. https://doi.org/10.1016/j.jsv.2007.10.024
24. Piron D, Pathak S, Deraemaeker A, Collette C (2021) A pole-zero based criterion for optimal placement of collocated sensor-actuator pair. Mech Syst Signal Process. https://doi.org/10.1016/j.ymssp.2020.107533
25. Richiedei D, Tamellin I, Trevisani A (2022) Unit-rank output feedback control for antiresonance assignment in lightweight systems. Mech Syst Signal Process. https://doi.org/10.1016/j.ymssp.2021.108250
26. Saldanha A, Michiels W, Kuře M, Bušek J, Vyhlídal T (2024) Stability optimization of time-delay systems with zero-location constraints applied to non-collocated vibration suppression. Mech Syst Signal Process. https://doi.org/10.1016/j.ymssp.2023.110886
27. Kawrza M, Furtmüller T, Adam C, Maderebner R (2022) Experimental modal analysis of a cross-laminated timber slab. Materialstoday: Proceedings 62:2611–2616. https://doi.org/10.1016/j.matpr.2022.04.559
28. Chillemi M, Furtmüller T, Adam C, Pirrotta A (2024) Fluid inerter-based vibration control of multi-modal structures subjected to vertical vibration. Eng Struct. https://doi.org/10.1016/j.engstruct.2024.117938
29. Wang X, Pereira E, Díaz IM, García-Palacios JH (2018) Velocity feedback for controlling vertical vibrations of pedestrian-bridge crossing: practical guidelines. Smart Struct Syst 22(1):95–103
30. Fujisaki, Y.: Optimality of simple dynamic displacement feedback for large space structures. In: Proceedings of the 2008 IEEE International Conference on Control Applications, pp. 1141–1144. IEEE, San Antonio, Texas, USA (2008). https://doi.org/10.1109/CCA.2008.4629709
31. Brandt A (2011) Noise and Vibration Analysis: Signal Analysis and Experimental Procedures. Wiley, United Kingdom
32. Avitabile P (2018) Modal Testing: A Practitioner's Guide. Wiley, USA
33. He J, Fu ZF (2001) Modal Analysis, 1st edn. Butterworth-Heinemann, Great Britain
34. Miu DK (1991) Physical interpretation of transfer function zeros for simple control systems with mechanical flexibilities. J Dyn Syst Meas Contr 113(3):419–424. https://doi.org/10.1115/1.2896426
35. Preumont A, François A, Bossens F, Abu-Hanieh A (2002) Force feedback versus acceleration feedback in active vibration isolation. J Sound Vib 257(4):605–613. https://doi.org/10.1006/jsvi.2002.5047
36. Preumont A (2006) Mechatronics: Dynamics of Electromechanical and Piezoelectric Systems, vol 136. Springer, Netherlands
37. The MathWorks, Inc.: MATLAB Function: Fminsearch, Version R2023b. https://www.mathworks.com/help/matlab/ref/fminsearch.html
38. Ewins DJ (1995) Modal Testing: Theory and Practice, 2nd edn. Research Studies Press Ltd., Somerset, England
39. Oppenheim AV, Willsky AS, Nawab SH (1996) Signals & Systems, 2nd edn. Prentice Hall, Upper Saddle River, NJ